

## New high-pressure phase and equation of state of Ce<sub>2</sub>Zr<sub>2</sub>O<sub>8</sub>

D. Errandonea, R. S. Kumar, S. N. Achary, O. Gomis, F. J. Manjón et al.

Citation: *J. Appl. Phys.* **111**, 053519 (2012); doi: 10.1063/1.3692807

View online: <http://dx.doi.org/10.1063/1.3692807>

View Table of Contents: <http://jap.aip.org/resource/1/JAPIAU/v111/i5>

Published by the [American Institute of Physics](#).

---

### Related Articles

Pressure effects on phase equilibria and solid solubility in MgO-Y<sub>2</sub>O<sub>3</sub> nanocomposites

*J. Appl. Phys.* **111**, 053506 (2012)

Effects of high pressure on the magnetism of ErCo<sub>2</sub>

*J. Appl. Phys.* **111**, 07E132 (2012)

Effect of pressure loading rate on the crystallographic texture of NdFeB nanocrystalline magnets

*J. Appl. Phys.* **111**, 07A717 (2012)

A fresh look at dense hydrogen under pressure. III. Two competing effects and the resulting intra-molecular H-H separation in solid hydrogen under pressure

*J. Chem. Phys.* **136**, 074503 (2012)

A reconstruction of cubic rs-ZnO on MgO (200) substrate through (100) plane of w-ZnO:rs-ZnO for transparent electronic application

*Appl. Phys. Lett.* **100**, 072102 (2012)

---

### Additional information on *J. Appl. Phys.*

Journal Homepage: <http://jap.aip.org/>

Journal Information: [http://jap.aip.org/about/about\\_the\\_journal](http://jap.aip.org/about/about_the_journal)

Top downloads: [http://jap.aip.org/features/most\\_downloaded](http://jap.aip.org/features/most_downloaded)

Information for Authors: <http://jap.aip.org/authors>

### ADVERTISEMENT



**FIND THE NEEDLE IN THE  
HIRING HAYSTACK**

Post jobs and reach  
thousands of hard-to-find  
scientists with specific skills



<http://careers.physicstoday.org/post.cfm> **physicstoday** JOBS

## New high-pressure phase and equation of state of $\text{Ce}_2\text{Zr}_2\text{O}_8$

D. Errandonea,<sup>1,a)</sup> R. S. Kumar,<sup>2</sup> S. N. Achary,<sup>3</sup> O. Gomis,<sup>4</sup> F. J. Manjón,<sup>5</sup> R. Shukla,<sup>3</sup> and A. K. Tyagi<sup>3</sup>

<sup>1</sup>MALTA Consolider Team, Departamento de Física Aplicada-ICMUV, Universidad de Valencia, Edificio de Investigación, c/Dr. Moliner 50, Burjassot, 46100 Valencia, Spain

<sup>2</sup>High Pressure Science and Engineering Center, Department of Physics and Astronomy, University of Nevada Las Vegas, 4505 Maryland Parkway, Las Vegas, Nevada 89154-4002, USA

<sup>3</sup>Chemistry Division, Bhabha Atomic Research Centre, Trombay, Mumbai 400085, India

<sup>4</sup>Centro de Tecnologías Físicas: Acústica, Materiales y Astrofísica, MALTA Consolider Team, Universitat Politècnica de València, 46022 València, Spain

<sup>5</sup>Instituto de Diseño para la Fabricación y Producción Automatizada, MALTA Consolider Team, Universitat Politècnica de Valencia, 46022 València, Spain

(Received 7 December 2011; accepted 9 February 2012; published online 8 March 2012)

In this paper we report a new high-pressure rhombohedral phase of  $\text{Ce}_2\text{Zr}_2\text{O}_8$  observed in high-pressure angle-dispersive x-ray diffraction and Raman spectroscopy studies up to nearly 12 GPa. The ambient-pressure cubic phase of  $\text{Ce}_2\text{Zr}_2\text{O}_8$  transforms to a rhombohedral structure beyond 5 GPa with a feeble distortion in the lattice. The pressure evolution of the unit-cell volume showed a change in compressibility above 5 GPa. The unit-cell parameters of the high-pressure rhombohedral phase at 12.1 GPa are  $a_h = 14.6791(3)$  Å,  $c_h = 17.9421(5)$  Å, and  $V = 3348.1(1)$  Å<sup>3</sup>. The structure relations between the parent cubic (P2<sub>1</sub>3) and rhombohedral (P3<sub>2</sub>) phases were obtained via group-subgroup relations. All the Raman modes of the cubic phase showed linear evolution with pressure, with the hardest one at 197 cm<sup>-1</sup>. Some Raman modes of the high-pressure phase have a non-linear evolution with pressure, and softening of one low-frequency mode with pressure is found. The compressibility, equation of state, and pressure coefficients of Raman modes of  $\text{Ce}_2\text{Zr}_2\text{O}_8$  are also reported. © 2012 American Institute of Physics. [<http://dx.doi.org/10.1063/1.3692807>]

### I. INTRODUCTION

$\text{A}_2\text{B}_2\text{O}_7$  pyrochlores are a subject of great interest due to their oxygen mobility<sup>1</sup> and catalytic properties,<sup>2</sup> as well as their potential use as a stable and robust host lattice for nuclear-waste immobilization<sup>3</sup> and inert-matrix fuel for nuclear technology.<sup>4</sup> The preferential coordination of A and B cations in pyrochlores restricts their ionic-radii ratio to the range of 1.46 to 1.8.<sup>5</sup> Thus, pyrochlores are formed only with cations of appropriate ionic radii and charge combinations. Smaller radii ratios favor an anion-deficient fluorite lattice, but this limit can be extended under high pressure (HP).<sup>6</sup> Among pyrochlores, rare-earth zirconates are being extensively investigated under HP because of interest in the use for nuclear-waste storage. Information obtained from these studies is also valuable regarding their use as a host lattice for transmutation products of reactors and the safe deposition of plutonium.<sup>3,7,8</sup> The high radiation and chemical stability and low neutron absorption coefficients of Zr make zirconate pyrochlores extremely useful for these purposes, but recent studies have found pressure-driven instabilities.<sup>9</sup> Structural transitions were reported for  $\text{Sm}_2\text{Zr}_2\text{O}_7$ ,  $\text{Gd}_2\text{Zr}_2\text{O}_7$ ,  $\text{Er}_2\text{Zr}_2\text{O}_7$ , and  $\text{Ho}_2\text{Zr}_2\text{O}_7$  at 15 to 30 GPa.<sup>10–12</sup> Studies on related  $\text{Y}_2\text{Zr}_2\text{O}_7$  indicated the formation of a defect-cotunnite structure at 18 GPa.<sup>13</sup> HP x-ray diffraction (XRD) and Raman studies of  $\text{La}_2\text{Hf}_2\text{O}_7$  revealed no phase transition and instead showed decomposition to the

constituent oxides.<sup>14</sup> Similar studies of  $\text{Gd}_2\text{Zr}_2\text{O}_7$  detected a monoclinic  $\text{La}_2\text{Ti}_2\text{O}_7$ -type phase at significantly lower pressure (~3 GPa).<sup>15</sup> HP studies of several analogs found pressure-induced amorphization.<sup>14,16–19</sup>

Though a number of studies exist on the HP behavior of rare-earth zirconate pyrochlores, few reports are available on  $\text{Ce}_2\text{Zr}_2\text{O}_7$ . Because cerium oxide ( $\text{CeO}_2$ ) is used as a surrogate material to simulate the thermo-physical properties of radioactive  $\text{PuO}_2$ , studies on cerium containing oxides are extremely important for nuclear technology. Recently, Surble *et al.*<sup>20</sup> investigated  $\text{Ce}_2\text{Zr}_2\text{O}_7$  and reported a structural transition at 20 GPa.  $\text{Ce}_2\text{Zr}_2\text{O}_7$  is a metastable material at ambient conditions and gradually oxidizes to  $\text{Ce}_2\text{Zr}_2\text{O}_{7+x}$  in air.<sup>21–23</sup> Studies on oxidized samples of  $\text{Ce}_2\text{Zr}_2\text{O}_7$  have revealed several new phases.<sup>24–29</sup> In particular,  $\text{Ce}_2\text{Zr}_2\text{O}_8$  exists as a cubic fluorite structure<sup>29,30</sup> or metastable tetragonal structures.<sup>31,32</sup>

It also is well known that the fluorite structure transforms to different crystalline modifications with pressure.<sup>33</sup> HP studies on  $\text{CeO}_2$  suggest a fluorite to orthorhombic  $\alpha\text{-PbCl}_2$ -type structure transition. The high-pressure phase relaxes to a hexagonal structure on decompression.<sup>34,35</sup> HP studies of  $\text{ZrO}_2$  and  $\text{HfO}_2$  indicate the formation of orthorhombic or monoclinic phases.<sup>35–37</sup> HP studies of columbite-type  $\text{ZrTiO}_4$  ( $\text{HfTiO}_4$ ) show the formation of baddeleyite-related HP phases above 9 (2.7) GPa.<sup>38</sup> The diverse possible structural transitions of fluorite, zirconia, and pyrochlore create more interest in the HP behavior of  $\text{Ce}_2\text{Zr}_2\text{O}_8$ , which represents a close combination of fluorite and pyrochlore. In order to

<sup>a)</sup>Author to whom correspondence should be addressed. Electronic mail: [daniel.errandonea@uv.es](mailto:daniel.errandonea@uv.es).

further understand the HP behavior of these structures, we have carried out high-pressure XRD and Raman studies on  $\text{Ce}_2\text{Zr}_2\text{O}_8$ . Its compressibility and equation of state (EOS) are obtained. In addition, we report a new nonquenchable HP phase of  $\text{Ce}_2\text{Zr}_2\text{O}_8$ .

## II. EXPERIMENTAL DETAILS

The  $\text{Ce}_2\text{Zr}_2\text{O}_8$  sample used in the experiments was prepared via a gel-combustion method from the corresponding metal nitrates [ $\text{Ce}(\text{NO}_3)_3 \cdot 6\text{H}_2\text{O}$ , 99.999%, Alfa Aesar;  $\text{ZrO}(\text{NO}_3)_2 \cdot x\text{H}_2\text{O}$ , 99.99%, Aldrich], using glycine as a fuel. The metal contents of the reactants were standardized by means of thermogravimetric analysis of the corresponding nitrates. Appropriate amounts of nitrates were mixed together in demineralized water, and a stoichiometric amount of glycine was added to the solution. A highly viscous gel was obtained via the slow dehydration of the solution at  $\sim 80^\circ\text{C}$  on a hot plate. When the temperature was raised further, the gel underwent an auto-ignition process, with the evolution of a large volume of gases, and finally was converted to voluminous powder. The light-yellow powder obtained was calcined at  $900^\circ\text{C}$  for about 4 h in order to remove any residual un-burned carbonaceous material. The calcined powder was pressed into pellets and heated at  $1400^\circ\text{C}$  for 48 h in a flowing atmosphere of argon- $\text{H}_2$  (8% v/v hydrogen in argon), with intermittent grinding. From powder XRD data, the black powder obtained after this treatment was confirmed as pyrochlore-type  $\text{Ce}_2\text{Zr}_2\text{O}_7$ . This powder was slowly heated to  $1000^\circ\text{C}$  for 5 h in air in order to completely oxidize all  $\text{Ce}^{3+}$  to  $\text{Ce}^{4+}$ . The bright-yellow oxidized product was characterized via XRD and neutron diffraction (ND), confirming the  $\text{Ce}_2\text{Zr}_2\text{O}_8$  composition. The XRD pattern at ambient temperature was recorded on a Panalytical X-Pert Pro powder x-ray diffractometer using  $\text{Cu K}_\alpha$  radiation. The ND data were recorded at the Dhruva research reactor, Trombay, Mumbai, India, using neutrons of wavelength  $1.249 \text{ \AA}$ .

For the HP studies, a finely ground powder sample was used. Synchrotron powder x-ray diffraction experiments were performed at up to 12.1 GPa. Pre-pressed pellets obtained from the powder were loaded in a  $100 \mu\text{m}$  hole of a rhenium gasket pre-indented to  $30 \mu\text{m}$  in a diamond-anvil cell (DAC) with diamond-culet sizes of  $300 \mu\text{m}$ . Ruby grains were loaded with the sample for pressure determination,<sup>39</sup> and neon (Ne) was used as the pressure-transmitting medium.<sup>40,41</sup> At pressures higher than 4 GPa (i.e., the solidification of Ne), the EOS of Ne was used to double check the pressure.<sup>42</sup> Differences in the measured pressure with different scales were always smaller than 0.2 GPa. Angle-dispersive x-ray diffraction (ADXRD) experiments were carried out at Sector 16-IDB of the HPCAT at the Advanced Photon Source with an incident wavelength of  $0.4246 \text{ \AA}$ . The monochromatic x-ray beam was focused down to  $(10 \times 10) \mu\text{m}^2$  using Kickpatrick-Baez mirrors. The images were collected using a MAR345 image plate located 350 mm away from the sample and then integrated and corrected for distortions using FIT2D.<sup>43</sup> The structural analyses and

refinements were performed using the POWDERCELL (Ref. 44) and FULLPROF-2000 (Ref. 45) program packages.

For high-pressure Raman spectroscopic studies, a pre-pressed powder sample, along with  $2 \mu\text{m}$  diameter ruby balls, was loaded in a pre-indented steel gasket with a  $200 \mu\text{m}$  diameter hole inside a DAC. A 16:3:1 methanol-ethanol-water mixture was used as the pressure-transmitting medium.<sup>40,46</sup> The pressure was determined by monitoring the shift in ruby fluorescence lines.<sup>39</sup> HP Raman measurements were performed in the backscattering geometry using a 632.8 nm HeNe laser and a Horiba Jobin Yvon LabRAM high-reflectance UV microspectrometer in combination with a thermoelectric-cooled multichannel CCD detector with a spectral resolution below  $2 \text{ cm}^{-1}$ .

## III. RESULTS AND DISCUSSION

The phase purity of  $\text{Ce}_2\text{Zr}_2\text{O}_8$  was confirmed via Rietveld refinement of the ND data. For its structure, we considered distinct positions for two Ce (*4a* and *12b* sites), two Zr (*4a* and *12b* sites), and eight oxygen atoms (four in *4a* and four in *12b* sites) in a cubic ( $\text{P}2_13$ ) lattice. The refined unit-cell parameters,  $a = 10.5444(2) \text{ \AA}$  and  $V = 1172.37(4) \text{ \AA}^3$ , agree with the literature.<sup>29</sup> The structure of  $\text{Ce}_2\text{Zr}_2\text{O}_8$  is represented in Fig. 1; its structural parameters are given in Table I. As mentioned above, the structure is closely related to the parent  $\text{Ce}_2\text{Zr}_2\text{O}_7$  pyrochlore, but the empty anion positions are filled with additional oxygen atoms. The cation and anion sites of  $\text{Ce}_2\text{Zr}_2\text{O}_7$  are split in  $\text{Ce}_2\text{Zr}_2\text{O}_8$  by lowering the symmetry from  $\text{Fd}\bar{3}m$  to  $\text{P}2_13$ . Cations form distorted  $\text{CeO}_8$  and  $\text{ZrO}_8$  polyhedra that are connected by shared edges as in fluorite.

XRD patterns recorded at different pressures are shown in Fig. 2. All the reflections in the XRD patterns recorded from ambient pressure to 5.1 GPa could be indexed on a primitive cubic lattice similar to the one observed at ambient pressure outside the DAC. The full patterns were further Rietveld refined to get the structural parameters. Typical observed and calculated diffraction patterns of  $\text{Ce}_2\text{Zr}_2\text{O}_8$  at a representative pressure are depicted in Fig. 3. The refined unit-cell parameters for cubic ( $\text{P}2_13$ )  $\text{Ce}_2\text{Zr}_2\text{O}_8$  at different pressures are listed in Table II. The XRD data obtained after further compression appear quite similar to the results for the  $\text{Ce}_2\text{Zr}_2\text{O}_8$  lattice, aside from weak peaks that emerge at  $8.34^\circ$ ,  $11.83^\circ$ ,  $12.87^\circ$ , and  $22.94^\circ$ . These peaks are marked in Fig. 2. They become prominent at 12.1 GPa. The Le Bail refinement of the XRD pattern using the space group  $\text{P}2_13$  can account for all the observed intense reflections. However, the weak new reflections remain un-indexed in the calculated pattern. The calculated cubic unit-cell parameters of these high-pressure XRD data are included in Table II. The parameters obtained through such refinement indicate that the structure is grossly cubic, and the weak reflections appear due to a feeble structural distortion in the lattice. The variation of the unit-cell volume with pressure is shown in Fig. 4. The linear and volume compressibilities of  $\text{Ce}_2\text{Zr}_2\text{O}_8$  within different pressure regions are given in Table II. The average axial compressibility ( $1.26 \times 10^{-3} \text{ GPa}^{-1}$ ) is comparable to that reported for  $\text{Ce}_2\text{Zr}_2\text{O}_7$  ( $1.3 \times 10^{-3} \text{ GPa}^{-1}$ ).<sup>19</sup> It

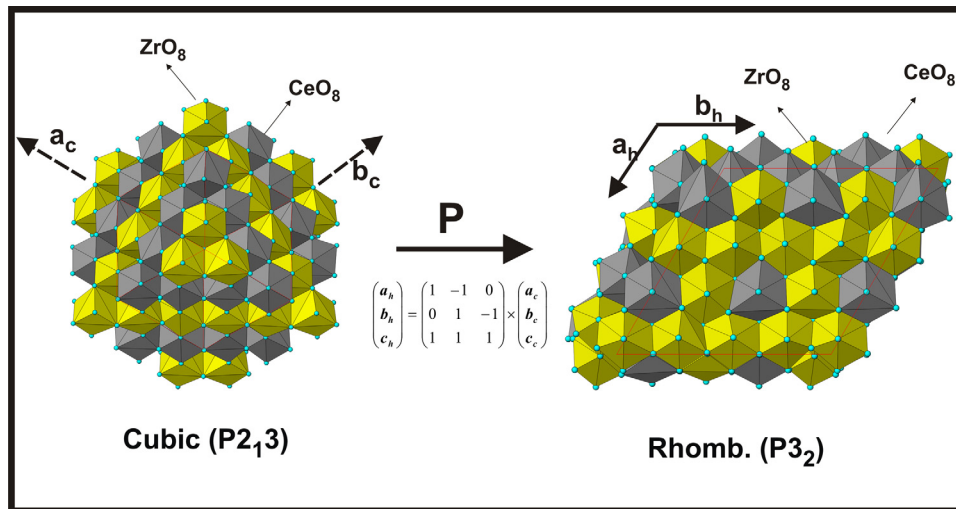


FIG. 1. (Color online) Schematic view of the room-temperature low-pressure (cubic) and high-pressure (rhombohedral) phases of  $\text{Ce}_2\text{Zr}_2\text{O}_8$ .

is also observed that the compressibilities calculated from the unit-cell parameters up to 5.1 GPa are higher than those calculated from the data beyond 5.1 GPa. This is also evident from the deviation in the variation of the unit-cell volume (Fig. 4). The pressure-volume data obtained from both pressure ranges were fitted with the third order Birch-Murnaghan EOS.<sup>47</sup>

$$P = \frac{3B_0}{2} \left[ \left( \frac{V_0}{V} \right)^{7/3} - \left( \frac{V_0}{V} \right)^{5/3} \right] \times \left( 1 + \frac{3}{4} (B'_0 - 4) \left( \left( \frac{V_0}{V} \right)^{2/3} - 1 \right) \right)$$

The obtained EOS parameters are  $V_0 = 1172(2) \text{ \AA}^3$ ,  $B_0 = 214(5) \text{ GPa}$ , and  $B'_0 = 8(1)$ , where  $V_0$  is the unit-cell volume at ambient pressure,  $B_0$  is the bulk modulus at ambient pressure, and  $B'_0$  is its pressure derivative. The bulk modulus is slightly larger than that of other pyrochlore-type zirconates summarized in Table III,<sup>14,15,20,48</sup> but significantly smaller than those of fluorite- and cotunnite-type lattices<sup>34</sup> (see Table III). A direct comparison with  $\text{Ce}_2\text{Zr}_2\text{O}_7$  cannot be made

TABLE I. Ambient pressure structural parameters as obtained from powder neutron-diffraction data of  $\text{Ce}_2\text{Zr}_2\text{O}_8$ .

Atoms	Wyckoff positions	x	y	z	B ( $\text{\AA}^2$ )
Ce <sub>1</sub>	4a	0.1355(16)	0.1355(16)	0.1355(16)	0.024
Ce <sub>2</sub>	12b	0.1353(16)	0.3647(16)	0.3676(16)	0.021
Zr <sub>1</sub>	4a	0.6311(10)	0.6311(10)	0.6311(10)	0.021
Zr <sub>2</sub>	12b	0.6232(10)	0.8748(11)	0.8670(8)	0.021
O <sub>1</sub>	4a	-0.0002(17)	-0.0002(17)	-0.0002(17)	0.090
O <sub>2</sub>	4a	0.2569(10)	0.2569(10)	0.2569(10)	0.090
O <sub>3</sub>	4a	0.5045(13)	0.5045(13)	0.5045(13)	0.090
O <sub>4</sub>	4a	0.7366(8)	0.7366(8)	0.7366(8)	0.090
O <sub>5</sub>	12b	0.2485(11)	0.2610(10)	0.0123(7)	0.090
O <sub>6</sub>	12b	0.2554(12)	0.2342(9)	0.5424(6)	0.090
O <sub>7</sub>	12b	-0.0039(12)	-0.0071(10)	0.2459(13)	0.090
O <sub>8</sub>	12b	-0.0044(12)	-0.0008(18)	0.7594(10)	0.090

because an unphysical value for  $B'_0$  is reported for its EOS.<sup>20</sup> The bulk-modulus enhancement in comparison with  $\text{A}_2\text{B}_2\text{O}_7$  pyrochlores can be attributed to the complete filling with oxygen of the vacant  $8a$  sites of the pyrochlore ( $\text{Fd}\bar{3}m$ ) lattice. The decrease relative to fluorites could be caused by the relatively lower packed lattice of  $\text{Ce}_2\text{Zr}_2\text{O}_8$ . The vacancy filling can be thought of as an internal pressure that makes  $\text{Ce}_2\text{Zr}_2\text{O}_8$

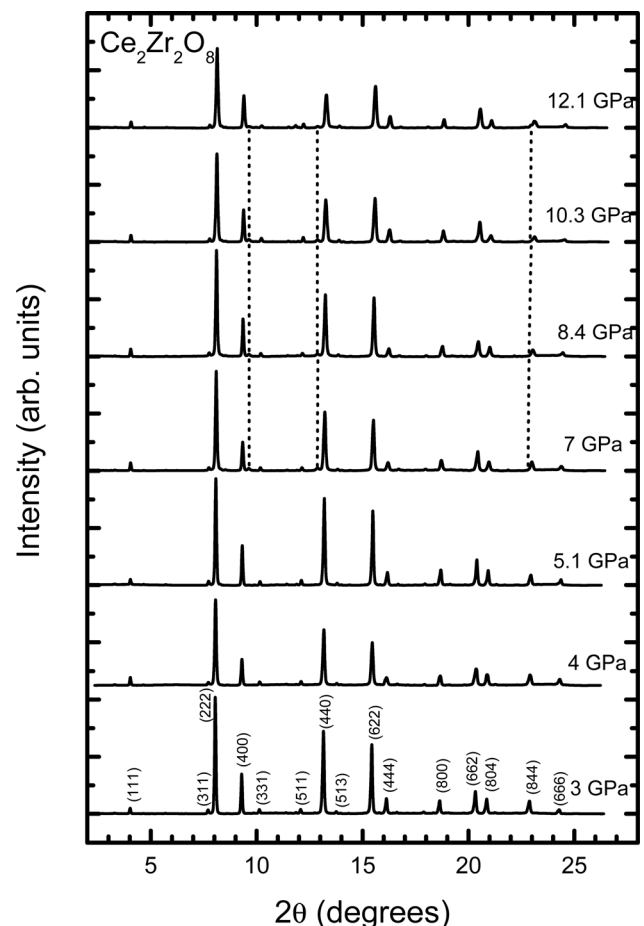


FIG. 2. XRD patterns of  $\text{Ce}_2\text{Zr}_2\text{O}_8$  at selected pressures. At 3 GPa, the most intense peaks of the low-pressure phase are labeled. Most intense peaks characteristic of the high-pressure phase are indicated with dotted lines.

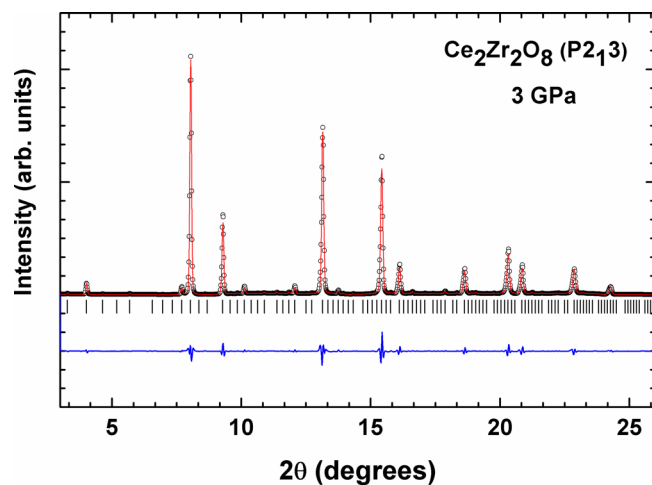


FIG. 3. (Color online) XRD pattern of  $\text{Ce}_2\text{Zr}_2\text{O}_8$  at 3 GPa, refined as cubic,  $P2_13$ ,  $a = 10.4936(1)$  Å. Experimental results (open circles) are shown together with the calculated patterns and residuals. Ticks indicate the positions of Bragg reflections.

behave like a compressed version of  $\text{Ce}_2\text{Zr}_2\text{O}_7$ , reducing the compressibility and the transition pressure. Another interesting fact to note is that a large  $B'_0$  has been observed for  $\text{Ce}_2\text{Zr}_2\text{O}_8$ , as well as for most pyrochlores studied so far. In the present case, this fact is a consequence of the compressibility change observed at the phase transition. This suggests that probably similar transitions (and compressibility changes) could take place in pyrochlores that have not been previously detected due to the subtle characteristics of the cubic-rhombohedral transition. A possible cause of the missing transition might be the use of a less hydrostatic pressure media than Ne.

Further analysis of the weak reflections in high-pressure XRD data confirms a phase transition in  $\text{Ce}_2\text{Zr}_2\text{O}_8$ . In most of the zirconate pyrochlores, structural transitions at high pressure ( $\sim 20$  GPa) have been reported. The phase-transition pressure ( $\sim 7$  GPa) observed in the present case is significantly lower than that expected for pyrochlore-type phases. The HP phases observed in pyrochlores are often explained by distorted defect-fluorite-type or cotunnite-type structures or monoclinically distorted  $\text{ZrO}_2$ -type or  $\text{La}_2\text{Ti}_2\text{O}_7$ -type structures.<sup>9,15,20</sup> The cation diffusion to form these structures can be expected and observed only at pres-

TABLE II. Unit cell parameters of  $\text{Ce}_2\text{Zr}_2\text{O}_8$  at different pressures and compressibilities ( $\kappa$ ) in  $\text{GPa}^{-1}$ .  $\kappa_x = (-1/x)(\partial x/\partial P)$ .

Pressure (GPa)	$a$ (Å)	$V$ (Å <sup>3</sup> )	$\kappa_a$ (GPa <sup>-1</sup> )	$\kappa_V$ (GPa <sup>-1</sup> )
Ambient	10.5444(2)	1172.34(4)		
3	10.4936(1)	1155.51(2)		
4	10.4772(1)	1150.09(2)		
5.1	10.4612(4)	1144.83(8)		
0–5.1 GPa			$1.54 \times 10^{-3}$	$4.60 \times 10^{-3}$
7	10.4412(2)	1138.27(4)		
8.4	10.4269(4)	1133.62(8)		
10.3	10.4036(2)	1126.04(4)		
12.1	10.3836(2)	1119.56(4)		
7–12.1 GPa			$1.08 \times 10^{-3}$	$3.22 \times 10^{-3}$
0–12.1 GPa			$1.26 \times 10^{-3}$	$3.72 \times 10^{-3}$

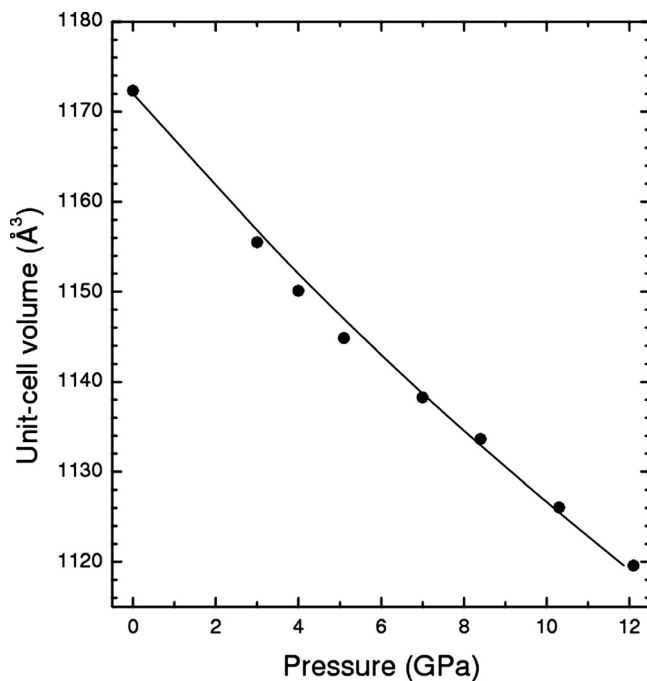


FIG. 4. Pressure-volume data of  $\text{Ce}_2\text{Zr}_2\text{O}_8$  (solid circles). The solid line represents the calculated EOS.

ures higher than 7 GPa. The transition at low pressure might be related to a distortion in the lattice without any significant redistribution of cations or anions. Thus, the HP phase transition in  $\text{Ce}_2\text{Zr}_2\text{O}_8$  might be related to a distortion in the lattice rather than any significant change in the frame of the lattice.

Further evidence of phase transition was obtained from HP Raman studies. The Raman spectra of  $\text{Ce}_2\text{Zr}_2\text{O}_8$  recorded at different pressures are shown in Fig. 5. The Raman spectrum at ambient pressure is quite similar to that reported previously by Matsuo *et al.*<sup>49</sup> According to group-theory analysis,  $\text{Ce}_2\text{Zr}_2\text{O}_8$  has 144 Raman active modes ( $\Gamma = 24$

TABLE III. Bulk modulus of related pyrochlores and fluorite-type materials.

Compositions	$B_0$ (GPa)	$B'_0$	Reference
$\text{Gd}_2\text{Zr}_2\text{O}_7$	186	...	11
$\text{Gd}_2\text{Zr}_2\text{O}_7$	153.4	10.5	11
$\text{La}_2\text{Hf}_2\text{O}_7$	147.2	7.9	14
$\text{La}_2\text{Hf}_2\text{O}_7$	179.3	4	14
$\text{CeO}_2$ fluorite	230	...	34
Nano $\text{CeO}_2$ fluorite	328	...	34
$\text{CeO}_2$ (cotunnite)	304	4	35
$\text{ZrO}_2$ (cotunnite)	332	2.3	35
$\text{Gd}_2\text{Zr}_2\text{O}_7$	161.5	9	15
$\text{Gd}_2\text{Zr}_2\text{O}_7$	156	7	20
$\text{Gd}_2\text{Zr}_2\text{O}_7$	154	8	20
$\text{Nd}_2\text{Zr}_2\text{O}_7$	145	11	20
$\text{Nd}_2\text{Zr}_2\text{O}_7$	140	14	20
$\text{Ce}_2\text{Zr}_2\text{O}_7$	252	0	20
$\text{Ce}_2\text{Zr}_2\text{O}_7$	255	0	20
$\text{La}_2\text{Zr}_2\text{O}_7$	200	...	48
$\text{La}_2\text{Hf}_2\text{O}_7$	207	...	48
$\text{Y}_2\text{Zr}_2\text{O}_7$	225	...	48
$\text{Y}_2\text{Hf}_2\text{O}_7$	238	...	48

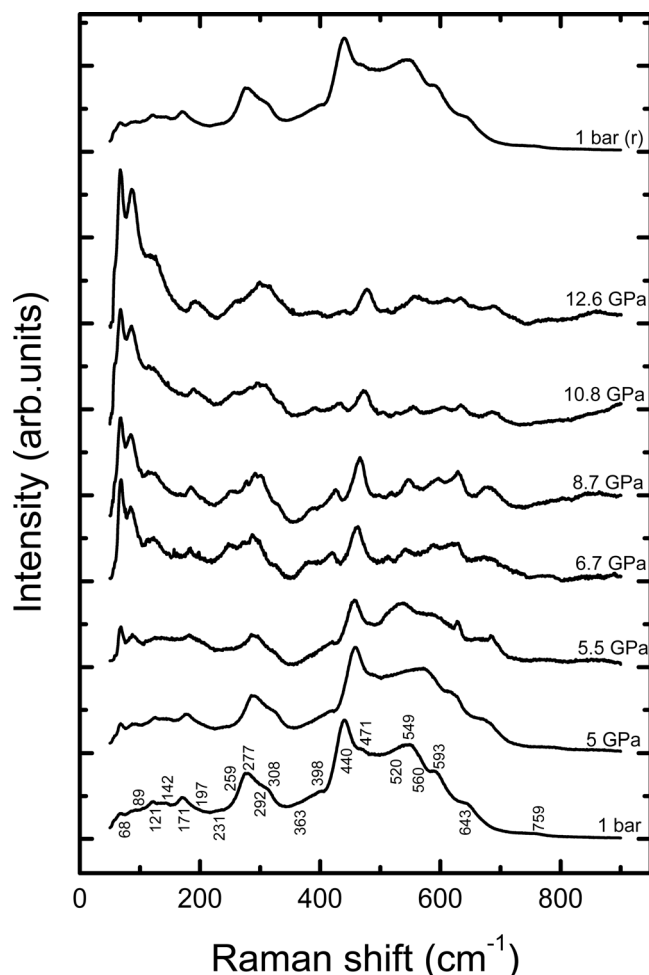


FIG. 5. Raman spectra of  $\text{Ce}_2\text{Zr}_2\text{O}_8$  at selected pressures. At ambient pressure, the phonons assigned are indicated. Changes in the spectra indicate the occurrence of a phase transition at 5.5 GPa. The upper trace shows the spectrum collected at ambient pressure after pressure release.

$A + 24 E^1 + 24 E^2 + 72 T$ ). Previously, only seven modes had been reported for cubic  $\text{Ce}_2\text{Zr}_2\text{O}_8$ .<sup>48</sup> Here, 21 modes could be assigned clearly at ambient pressure (marked in Fig. 5). The pressure evolution of the Raman spectra indicates the appearance of new bands above 5.5 GPa (see the spectra measured at 5 and 5.5 GPa in Fig. 5), in addition to the bands observed at ambient pressure. The intensities of these new bands gradually increase upon compression. From 6.7 to 12.6 GPa, the Raman spectra can be assigned to the HP phase. The transition is thought to be reversible based on the similarity of the pressure-released Raman spectrum and the original ambient-pressure spectrum. This further supports the observed phase transition in XRD studies.

Systematic HP studies on pyrochlore-type  $A_2B_2O_7$  lattices commonly indicate pyrochlore ( $Fd\bar{3}m$ ) to defect-fluorite-type ( $Fm\bar{3}m$ ) or defect-cotunnite-type ( $Pnma$ ) transitions. They are observed with concomitant cation disordering and, finally, as a geometrically frustrated amorphous phase. A transition induced by structural distortion at low pressure, viz., 3 GPa, has been reported only in  $\text{Gd}_2\text{Zr}_2\text{O}_7$ .<sup>15</sup> Systematic studies of fluorite-type lattices also indicate the structural instability of fluorite structures and a transformation from cubic fluorite-type to cotunnite-type lattices at higher pressures. HP studies

of cubic  $\text{CeO}_2$  indicate that a structural transition to an orthorhombic  $\text{PbCl}_2$ -type lattice occurs at 31 GPa.<sup>50,51</sup> The same transition is reported in nanocrystalline  $\text{CeO}_2$  at 22.3 GPa.<sup>34,35</sup> A large volume collapse with an increase in coordination number in the metal ions is observed at this transition. The pressure-induced orthorhombic columbite-type  $\text{ZrTiO}_4$  and  $\text{HfTiO}_4$  transition to monoclinic baddeleyite-type structures occurs at relatively lower pressure.<sup>37</sup> The monoclinic baddeleyite-type  $\text{ZrO}_2$  transforms to orthorhombic cotunnite-type  $\text{ZrO}_2$  at high pressure.<sup>36</sup> Leger *et al.* have reported the sequence of structural transitions as baddeleyite-orthorhombic-I ( $Pbca$ )-orthorhombic-II-orthorhombic-III, occurring at room temperature at around 10, 25, and 42 GPa, respectively.<sup>35</sup> Thus, it is not uncommon to expect a pressure-induced structural distortion in  $\text{Ce}_2\text{Zr}_2\text{O}_8$ . The change in compressibility and the appearance of new peaks in XRD and Raman data clearly suggest a phase transition in  $\text{Ce}_2\text{Zr}_2\text{O}_8$ .

Refinement of the XRD data obtained at 12.1 GPa shows a clear difference from that of the parent cubic  $\text{Ce}_2\text{Zr}_2\text{O}_8$  (Fig. 6). The weak reflection observed at  $11.83^\circ$  can be assigned to a (111) reflection of solid Ne.<sup>42</sup> The analysis of other extra reflections that are weak did not yield data that could attribute those reflection to any  $\text{CeO}_2$  or  $\text{ZrO}_2$  ambient or high-pressure phases (or their superstructures). The transformation of zirconate pyrochlores to defect fluorite-type and defect cotunnite-type phases generally involves the appearance of a satellite reflection adjacent to the intense (222) reflections.<sup>9</sup> However, the appearance of other extra reflections and the prominent peak at  $22.9^\circ$  could not be accounted for by such phases. Thus, we understand that the weak reflections originate from a feeble structural distortion of cubic  $\text{Ce}_2\text{Zr}_2\text{O}_8$ .

In order to study the new phase formed at HP, we tried to index all the reflections, including the weak ones observed at 12.1 GPa. They could be indexed on a hexagonal lattice with lattice parameters  $a_h = 14.674(9)$  Å and  $c_h = 17.83(3)$  Å. The observed unit-cell parameters are quite similar to those of a rhombohedral lattice reported by Thomson *et al.* ( $R\bar{3}m$ ,  $a_r = 10.5439$  Å and  $c_r = 90.05^\circ$ ;  $a_h = 14.9178$  Å and  $c_h = 18.2466$  Å) for oxygen-rich  $\text{Ce}_2\text{Zr}_2\text{O}_{7.97}$ .<sup>25</sup> This rhombohedral phase also has been prepared via the slow oxidation of pyrochlore-type  $\text{Ce}_2\text{Zr}_2\text{O}_7$ , similar to the preparation of  $\text{Ce}_2\text{Zr}_2\text{O}_8$  in this study. The cations usually do not diffuse under such mild oxidation conditions, but the anions are filled in the empty fluorite equivalent sites. It can be mentioned here that the observed unit-cell parameters can be related to the parent cubic unit-cell parameters via matrix transformation as

$$\begin{pmatrix} a_h \\ b_h \\ c_h \end{pmatrix} = \begin{pmatrix} 1 & -1 & 0 \\ 0 & 1 & -1 \\ 1 & 1 & 1 \end{pmatrix} \times \begin{pmatrix} a_c \\ b_c \\ c_c \end{pmatrix},$$

where  $a_h = b_h$  and  $c_h$  are hexagonal parameters of the transformed unit cell and  $a_c = b_c = c_c$  are parent cubic unit-cell parameters.

Using the present observed unit-cell parameters with the space group and position coordinates reported by Thomson *et al.* for  $\text{Ce}_2\text{Zr}_2\text{O}_{7.97}$  (Ref. 25), we tried to model the XRD

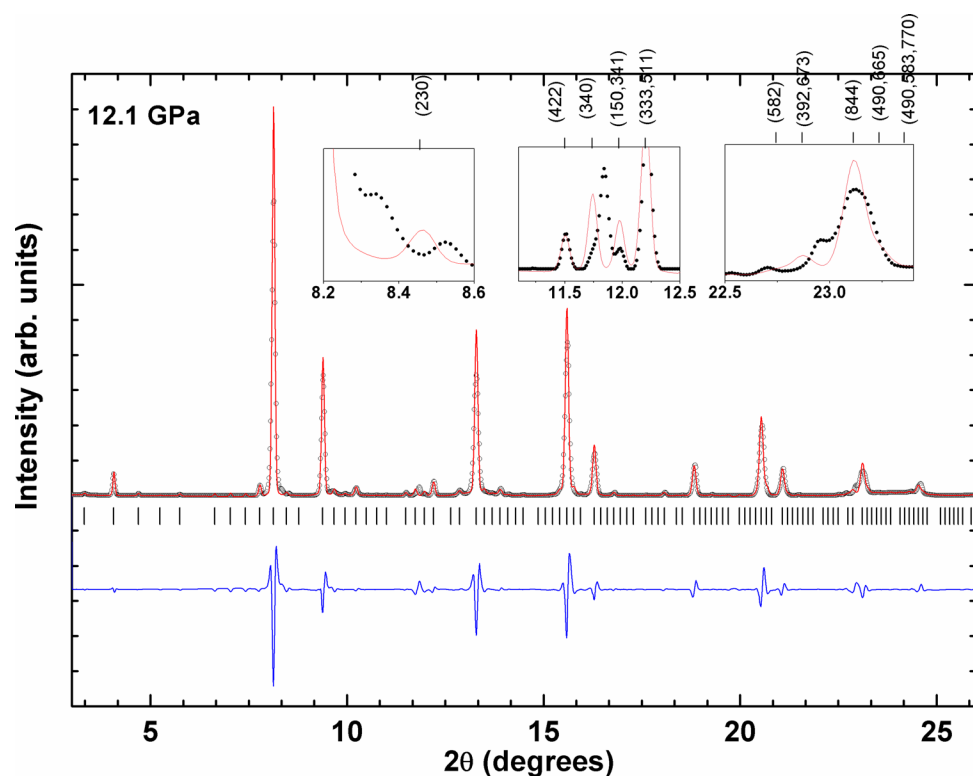


FIG. 6. (Color online) XRD pattern of  $\text{Ce}_2\text{Zr}_2\text{O}_8$  at 12.1 GPa, refined as cubic,  $P2_13$ ,  $a = 10.3836(2)$  Å. Differences at the new weak peaks are shown in the inset. The peak at 11.8 can be attributed to neon (111) reflection.

pattern observed at 12.1 GPa. However, the weak reflections observed at  $8.34^\circ$  and  $22.9^\circ$  were excluded from the indexed results, which suggests the absence of rhombohedral (R) centering. Thus the model structure for the observed HP phase was generated by group-subgroup relations from the  $P2_13$  lattice of  $\text{Ce}_2\text{Zr}_2\text{O}_8$ . Excluding the R-centered subgroup of the  $P2_13$  lattice, three possible subgroups, namely,  $P3$ ,  $P3_1$ ,

and  $P3_2$ , could be assigned to the HP phase of  $\text{Ce}_2\text{Zr}_2\text{O}_8$ . The Le Bail refinement of the observed XRD data using  $P3_2$  showed a good profile match in all the reflections (Fig. 7). The residuals of the refinement are  $R_p = 4.4\%$ ,  $R_{wp} = 6.7\%$ , and  $\chi^2 = 0.4$ . The obtained unit-cell parameters are  $a_h = 14.6791(3)$  Å,  $c_h = 17.9421(5)$  Å, and  $V = 3348.1(1)$  Å<sup>3</sup>. There is no volume change between the cubic and

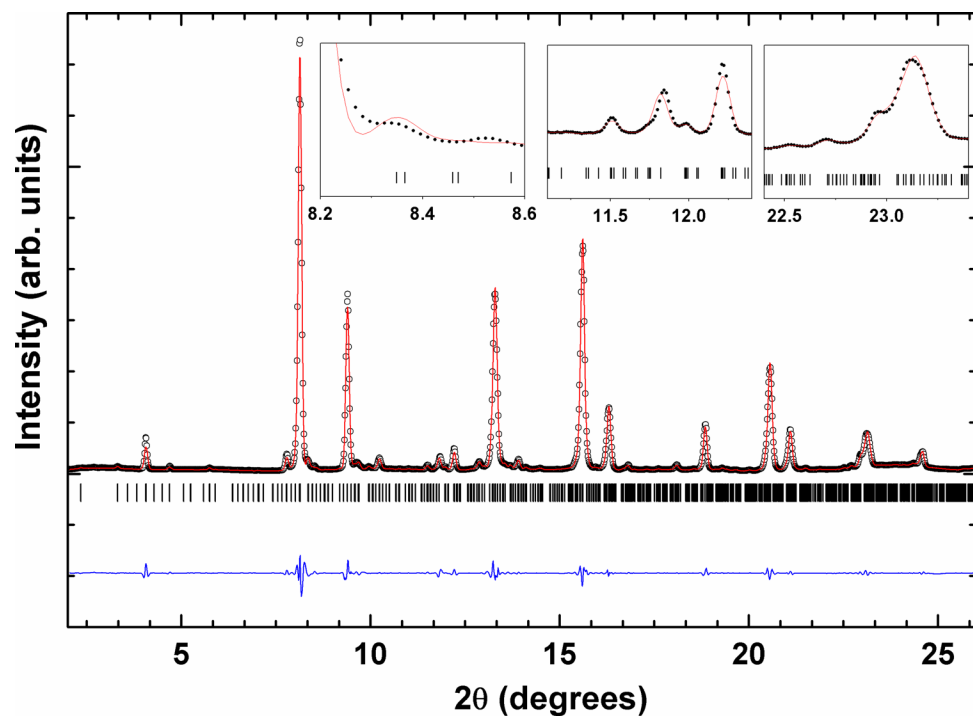


FIG. 7. (Color online) XRD pattern of  $\text{Ce}_2\text{Zr}_2\text{O}_8$  at 12.1 GPa, refined as rhombohedral,  $P3_2$ ,  $a = 14.6791(3)$  Å,  $c = 17.9421(5)$  Å. Neon (111) overlaps with the peaks from the rhombohedral  $\text{Ce}_2\text{Zr}_2\text{O}_8$ .

rhombohedral structures. The structure of the HP phase is schematically represented in Fig. 1.

Considering the close relation between the parent cubic lattice and the transformed rhombohedral ( $P3_2$ ) lattice, it can be suggested that the unit cell contains 24 units of  $Ce_2Zr_2O_8$ . The structural model for the rhombohedral lattice is proposed based on the equivalent position coordinates generated using the transformation matrix. Similar to the cubic lattice, all the metal ions in the rhombohedral lattice retain the cubic coordination with oxide ions. Full structural refinement of the powder XRD data collected from the DAC is usually difficult. In addition, the present proposed structure contains a large number of atoms in asymmetric sites, which makes the analysis even more difficult. Therefore, we have imposed a constrained refinement in which all the metal atoms have cubical coordination by bond length as obtained in the derived structure model. The background, profile parameters, and unit-cell parameters obtained from the Le Bail refinement were used for Rietveld refinements. We consider 16 Ce, 16 Zr, and 64 oxygen atoms in the general  $3a$  positions of space group  $P3_2$ . Only one overall thermal parameter was used for the refinement. The position coordinates of heavier Ce atoms were refined first, and subsequently the Zr and oxygen atoms were added in the refinement. The final Rietveld refinement plot shows small intensity differences in the fundamental reflections, which suggests that the grains are oriented in the DAC. This is consistent with the fact that collected patterns for the HP phase tended to be rather spotty. Overall, the refinement could provide satisfactory structural parameters. The refined structural parameters are given in Table IV.

Before closing the discussion of the crystalline structure of the HP rhombohedral phase, we would like to comment on the essential difference between it and the rhombohedral structure obtained at ambient pressure by oxidation.<sup>25</sup> The anion filled rhombohedral pyrochlore phase reported by Thomson *et al.*<sup>25</sup> has a  $Ce_2Zr_2O_{7.97}$  composition. Also, it has been reported that the samples appear to be close to yellow-orange in color, which has been attributed to the incomplete oxidation of  $Ce^{3+}$ , as the oxidation is carried out at a relatively low temperature. In the present study, the color of the sample is bright yellow, which is the typical color of a fully oxidized sample.<sup>27-29</sup> The structures of the anion filled pyrochlores are highly similar, and all of them are related to the parent cubic pyrochlore lattice.

The ambient pressure rhombohedral phase has been explained with 4 Ce, 4 Zr, and 11 O atoms. Several under-occupied sites for tetrahedral anions and a new under-occupied trigonal site are present in this structure. In addition, the ambient rhombohedral structure involves trigonal sites equivalent to the  $32e$  sites of the cubic pyrochlore lattice, which are displaced anions of the normal  $8b$  oxygen site. The rhombohedral structure of the high-pressure polymorph is more closely related to the cubic ( $P2_13$ ) phase in which no displaced anions are involved. The splitting of  $8a$  vacant sites and other cation and anion sites of the parent cubic ( $Fd\bar{3}m$ )  $Ce_2Zr_2O_7$  is observed in the cubic ( $P2_13$ ) structure. The present reported HP rhombohedral structures have anion sites equivalent to normal anion sites of the  $Fd\bar{3}m$  lattice. In both ambient- and high-pressure rhombohedral structures, the cation polyhedra are

TABLE IV. Position coordinates of rhombohedral  $Ce_2Zr_2O_8$  ( $P3_2$ , No. 145) as obtained from the transformed cubic cell. Unit-cell parameters were obtained from Le Bail refinements  $a_h = 14.6791 \text{ \AA}$ ,  $c_h = 17.9421 \text{ \AA}$ ,  $V = 3348.13 \text{ \AA}^3$ ,  $Z = 24$ .

Atoms	Wyckoff positions	x	y	z	Occupation
Ce <sub>1</sub>	3a	0.333(3)	0.333(3)	0.129(2)	1
Ce <sub>2</sub>	3a	0.082(3)	0.331(3)	0.626(2)	1
Ce <sub>3</sub>	3a	0.338(3)	0.086(3)	0.626(2)	1
Ce <sub>4</sub>	3a	0.581(3)	0.585(3)	0.626(2)	1
Ce <sub>5</sub>	3a	0.171(3)	0.251(3)	0.290(2)	1
Ce <sub>6</sub>	3a	0.416(3)	0.254(3)	0.291(2)	1
Ce <sub>7</sub>	3a	0.414(3)	0.497(3)	0.290(2)	1
Ce <sub>8</sub>	3a	0.082(3)	0.087(3)	0.626(2)	1
Ce <sub>9</sub>	3a	0.581(3)	0.329(3)	0.626(2)	1
Ce <sub>10</sub>	3a	0.339(3)	0.586(3)	0.626(2)	1
Ce <sub>11</sub>	3a	0.583(3)	0.830(3)	0.624(2)	1
Ce <sub>12</sub>	3a	0.838(3)	0.088(3)	0.624(2)	1
Ce <sub>13</sub>	3a	0.579(3)	0.085(3)	0.624(2)	1
Ce <sub>14</sub>	3a	0.499(3)	0.167(3)	0.464(2)	1
Ce <sub>15</sub>	3a	0.500(3)	0.665(3)	0.464(2)	1
Ce <sub>16</sub>	3a	0.002(3)	0.168(3)	0.464(2)	1
Zr <sub>1</sub>	3a	0.334(2)	0.334(2)	0.6277(16)	1
Zr <sub>2</sub>	3a	0.749(2)	0.664(2)	0.4580(17)	1
Zr <sub>3</sub>	3a	0.003(2)	0.418(2)	0.4581(17)	1
Zr <sub>4</sub>	3a	0.249(2)	0.919(2)	0.4582(17)	1
Zr <sub>5</sub>	3a	0.170(2)	0.253(2)	0.7891(17)	1
Zr <sub>6</sub>	3a	0.414(2)	0.250(2)	0.7888(17)	1
Zr <sub>7</sub>	3a	0.417(2)	0.498(2)	0.7891(17)	1
Zr <sub>8</sub>	3a	0.752(2)	0.422(2)	0.4580(17)	1
Zr <sub>9</sub>	3a	0.245(2)	0.663(2)	0.4578(17)	1
Zr <sub>10</sub>	3a	0.004(2)	0.916(2)	0.458(2)	1
Zr <sub>11</sub>	3a	0.250(2)	0.162(2)	0.4607(17)	1
Zr <sub>12</sub>	3a	0.506(2)	0.421(2)	0.4604(17)	1
Zr <sub>13</sub>	3a	0.246(2)	0.417(2)	0.4605(17)	1
Zr <sub>14</sub>	3a	0.163(2)	0.496(2)	0.2949(16)	1
Zr <sub>15</sub>	3a	0.172(2)	0.000(2)	0.2946(17)	1
Zr <sub>16</sub>	3a	0.666(2)	0.504(2)	0.2949(16)	1
O <sub>1a</sub>	3a	0.335(5)	0.332(5)	0.000(3)	1
O <sub>1b</sub>	3a	0.499(5)	0.168(5)	0.337(3)	1
O <sub>1c</sub>	3a	0.497(5)	0.666(5)	0.337(3)	1
O <sub>1d</sub>	3a	0.002(5)	0.166(5)	0.336(3)	1
O <sub>2a</sub>	3a	0.333(5)	0.335(5)	0.256(3)	1
O <sub>2b</sub>	3a	0.998(5)	0.162(5)	0.584(3)	1
O <sub>2c</sub>	3a	0.506(5)	0.171(5)	0.584(3)	1
O <sub>2d</sub>	3a	0.498(5)	0.670(5)	0.585(3)	1
O <sub>3a</sub>	3a	0.334(3)	0.334(3)	0.505(2)	1
O <sub>3b</sub>	3a	0.831(3)	0.828(3)	0.498(2)	1
O <sub>3c</sub>	3a	0.840(3)	0.336(3)	0.499(2)	1
O <sub>3d</sub>	3a	0.330(3)	0.836(3)	0.499(2)	1
O <sub>4a</sub>	3a	0.334(4)	0.334(4)	0.736(2)	1
O <sub>4b</sub>	3a	0.677(3)	0.519(3)	0.422(2)	1
O <sub>4c</sub>	3a	0.148(3)	0.491(3)	0.422(2)	1
O <sub>4d</sub>	3a	0.177(3)	0.991(3)	0.422(2)	1
O <sub>5a</sub>	3a	0.084(4)	0.846(4)	0.499(3)	1
O <sub>5b</sub>	3a	0.821(4)	0.572(4)	0.499(3)	1
O <sub>5c</sub>	3a	0.095(4)	0.583(4)	0.498(3)	1
O <sub>5d</sub>	3a	0.092(4)	0.341(4)	0.494(3)	1
O <sub>5e</sub>	3a	0.326(4)	0.085(4)	0.494(3)	1
O <sub>5f</sub>	3a	0.583(4)	0.574(4)	0.494(3)	1
O <sub>5g</sub>	3a	0.409(5)	0.494(4)	0.676(2)	1
O <sub>5h</sub>	3a	0.173(4)	0.250(5)	0.676(2)	1
O <sub>5i</sub>	3a	0.418(5)	0.258(5)	0.675(2)	1
O <sub>5j</sub>	3a	0.747(5)	0.654(4)	0.335(3)	1

TABLE IV. (Continued.)

Atoms	Wyckoff positions	x	y	z	Occupation
O <sub>5k</sub>	3a	0.014(4)	0.428(5)	0.335(3)	1
O <sub>5l</sub>	3a	0.240(5)	0.919(5)	0.335(3)	1
O <sub>6a</sub>	3a	0.245(4)	0.135(3)	0.341(2)	1
O <sub>6b</sub>	3a	0.531(4)	0.444(5)	0.341(3)	1
O <sub>6c</sub>	3a	0.224(5)	0.422(5)	0.341(3)	1
O <sub>6d</sub>	3a	0.229(5)	0.646(4)	0.352(2)	1
O <sub>6e</sub>	3a	0.021(4)	0.917(5)	0.351(5)	1
O <sub>6f</sub>	3a	0.750(5)	0.438(5)	0.352(2)	1
O <sub>6g</sub>	3a	0.268(3)	0.185(4)	0.814(4)	1
O <sub>6h</sub>	3a	0.481(4)	0.416(4)	0.814(4)	1
O <sub>6i</sub>	3a	0.251(4)	0.399(3)	0.814(4)	1
O <sub>6j</sub>	3a	0.592(4)	0.366(5)	0.495(3)	1
O <sub>6k</sub>	3a	0.301(5)	0.559(4)	0.495(3)	1
O <sub>6l</sub>	3a	0.109(4)	0.076(4)	0.495(3)	1
O <sub>7a</sub>	3a	0.579(4)	0.829(4)	0.748(3)	1
O <sub>7b</sub>	3a	0.838(4)	0.083(4)	0.747(3)	1
O <sub>7c</sub>	3a	0.583(4)	0.087(4)	0.747(3)	1
O <sub>7d</sub>	3a	0.421(4)	0.004(4)	0.423(3)	1
O <sub>7e</sub>	3a	0.664(4)	0.751(4)	0.423(3)	1
O <sub>7f</sub>	3a	0.916(4)	0.246(4)	0.423(3)	1
O <sub>7g</sub>	3a	0.090(5)	0.336(4)	0.252(3)	1
O <sub>7h</sub>	3a	0.332(4)	0.088(4)	0.251(3)	1
O <sub>7i</sub>	3a	0.579(4)	0.577(5)	0.251(3)	1
O <sub>7j</sub>	3a	0.245(4)	0.166(4)	0.582(3)	1
O <sub>7k</sub>	3a	0.501(4)	0.411(5)	0.582(3)	1
O <sub>7l</sub>	3a	0.257(5)	0.424(4)	0.582(3)	1
O <sub>8a</sub>	3a	0.739(4)	0.154(4)	0.588(3)	1
O <sub>8b</sub>	3a	0.513(4)	0.919(4)	0.588(3)	1
O <sub>8c</sub>	3a	0.749(4)	0.929(4)	0.588(3)	1
O <sub>8d</sub>	3a	0.583(4)	0.324(4)	0.258(3)	1
O <sub>8e</sub>	3a	0.343(4)	0.594(4)	0.257(3)	1
O <sub>8f</sub>	3a	0.073(4)	0.082(4)	0.258(3)	1
O <sub>8g</sub>	3a	0.927(4)	0.015(4)	0.416(3)	1
O <sub>8h</sub>	3a	0.652(4)	0.245(4)	0.415(3)	1
O <sub>8i</sub>	3a	0.422(4)	0.740(4)	0.416(3)	1
O <sub>8j</sub>	3a	0.419(4)	0.509(4)	0.410(3)	1
O <sub>8k</sub>	3a	0.158(4)	0.244(4)	0.409(3)	1
O <sub>8l</sub>	3a	0.424(4)	0.248(4)	0.409(3)	1

distorted. In the ambient-pressure structure, some of the metal ions show coordination numbers greater than eight, with a wider dispersion of bond lengths, viz., Ce-O bonds in the range of 2.03–2.70 Å and Zr-O bonds in the range of 2.04–2.41 Å. However, in the HP structure, all the metal ions retain cubic coordination with oxide ions, with the eight Ce-O bonds being in the 2.25–2.48 Å range and the eight Zr-O bonds being in the 2.05–2.26 Å range; i.e., the polyhedral units are comparatively less distorted than in the ambient rhombohedral phase. The HP structure retains the polyhedral framework of the cubic phase, with only gradual distortions of polyhedra being induced by the displacive transition.

To close this work, we here provide additional information on the pressure evolution of the Raman spectra. From the measured spectra, we obtained the pressure evolution of the Raman modes for the low- and high-pressure phases. Our results are summarized in Fig. 8. All modes show a linear evolution upon compression, with the high-frequency modes

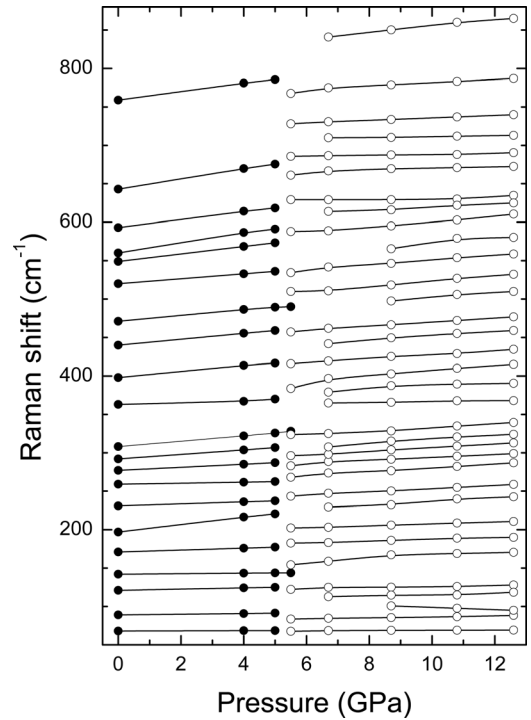


FIG. 8. Raman modes of low- and high-pressure phases of  $\text{Ce}_2\text{Zr}_2\text{O}_8$  as a function of pressure. Solid symbols: cubic phase. Open symbols: rhombohedral phase. Solid lines are linear fits in the low-P phase. B-spline curves are used for the HP phase.

being the hardest modes and the mode located at 197  $\text{cm}^{-1}$ . None of the modes has soft-mode behavior. In Table V we report the Raman frequencies ( $\omega$ ) and pressure coefficients ( $d\omega/dP$ ) obtained for each mode. The mode Grüneisen parameters are calculated by the relation  $\gamma = (B_0/\omega)d\omega/dP$  using  $B_0 = 214$  GPa, and they are given in Table V. For the HP phase, we found an increase in the number of Raman modes, which is consistent with the cubic-to-rhombohedral symmetry decrease associated with the phase transition. In total, we detected 34 Raman-active phonons. Most of them have an evolution similar to that of the phonons of the low-pressure phase. They are also located in the same frequency region. Both facts are consistent with the structural

TABLE V. Ambient-pressure Raman frequencies ( $\omega$ ), pressure coefficients ( $d\omega/dP$ ), and mode Grüneisen parameters ( $\gamma$ ) for the cubic phase of  $\text{Ce}_2\text{Zr}_2\text{O}_8$ .

$\omega$ ( $\text{cm}^{-1}$ )	$d\omega/dP$ ( $\text{cm}^{-1}/\text{GPa}$ )	$\gamma$	$\omega$ ( $\text{cm}^{-1}$ )	$d\omega/dP$ ( $\text{cm}^{-1}/\text{GPa}$ )	$\gamma$
68	0.10	0.31	363	1.38	0.81
89	0.45	1.08	398	3.74	2.01
121	0.78	1.38	440	3.78	1.84
142	0.34	0.51	471	3.66	1.66
171	1.25	1.56	520	3.24	1.33
197	4.70	5.11	549	4.86	1.89
231	1.25	1.16	560	6.22	2.38
259	0.70	0.58	593	5.08	1.83
277	2.02	1.56	643	6.50	2.16
292	2.94	2.15	759	5.30	1.49
308	3.54	2.46			

TABLE VI. Raman frequencies and pressure coefficients for the rhombohedral phase of  $\text{Ce}_2\text{Zr}_2\text{O}_8$  determined at 8.7 GPa.

$\omega$ ( $\text{cm}^{-1}$ )	$d\omega/dP$ ( $\text{cm}^{-1}/\text{GPa}$ )	$\omega$ ( $\text{cm}^{-1}$ )	$d\omega/dP$ ( $\text{cm}^{-1}/\text{GPa}$ )	$\omega$ ( $\text{cm}^{-1}$ )	$d\omega/dP$ ( $\text{cm}^{-1}/\text{GPa}$ )
68.8	0.10	303.8	2.33	565.4	3.89
85.4	0.76	315.2	2.27	595.2	3.92
120.7	-1.45	328.4	2.85	616	2.32
114.7	0.95	365.8	0.57	629.3	1.38
125.2	0.71	387.5	0.75	669.6	0.74
167.4	0.79	402.7	3.16	687.5	0.73
186.1	1.01	425.2	2.39	710.3	0.69
206	1.21	449.5	2.44	733.7	1.61
232.4	2.64	466.5	2.62	778.8	2.10
250.2	2.18	497.5	3.18	850.2	3.82
276.6	2.62	518.3	3.61		
291.5	1.92	546.4	3.17		

similitude between the low- and high-pressure phases. The frequencies and pressure coefficients are summarized in Table VI. It is interesting to note that in the HP phase we found a few modes that followed a non-linear evolution upon compression, and at least one mode at low frequencies that softened under compression (see Fig. 8 and Table VI). These findings could be related to mechanical instability of the HP phase, suggesting the possible occurrence of further transitions at higher pressures.

#### IV. CONCLUDING REMARKS

A systematic HP study of cubic  $\text{Ce}_2\text{Zr}_2\text{O}_8$ , an oxygen-filled pyrochlore analog, was performed. HP ADXRD studies were carried out in a diamond-anvil cell using synchrotron x-ray and with Ne as the pressure-transmitting medium. HP Raman studies were carried out in a DAC using methanol-ethanol-water as the pressure-transmitting medium. In both experiments, we observed a reversible cubic-to-rhombohedral structural transition above 5 GPa. The structural details of the HP rhombohedral phase were obtained via a group-subgroup relation. The structural transition observed in this study is different from that usually observed in pyrochlore-type or fluorite-type materials. The HP rhombohedral phase also differs from ambient-pressure rhombohedral oxygen-rich  $\text{Ce}_2\text{Zr}_2\text{O}_{7.97}$ . We think that this transition, not previously observed in related compounds, is produced by a mechanical stress-induced distortion in the lattice. All the Raman modes detected for the cubic phase at ambient pressure showed a linear evolution with pressure, whereas some of the Raman modes of the HP phase showed a non-linear evolution, and one mode even softened with increasing pressure.

#### ACKNOWLEDGMENTS

The authors are thankful for financial support from Spanish MICCIN (Grant Nos. MAT2010-21270-C04-01/04 and CSD2007-00045). This work was performed at HPCAT, Advanced Photon Source (APS), Argonne National Laboratory. HPCAT is supported by CIW, CDAC, UNLV, and

LLNL through funding from DOE-NNSA, DOE-BES, and NSF. APS is supported by DOE-BES under DEAC02-06CH11357. The UNLV HPSEC is supported by the U.S. DOE, National Nuclear Security Administration, under DE-FC52-06NA26274. S.N. Achary acknowledges the VLC Campus visitors program "Atracció de Talent" for supporting his stay as guest scientist at the Universidad de Valencia.

- <sup>1</sup>B. J. Wuensch, K. W. Eberman, C. Heremans, E. M. Ku, P. Onnerud, E. M. E. Yeo, S. M. Haile, J. K. Stalick, and J. D. Jorgensen, *Solid State Ionics* **129**, 111 (2000).
- <sup>2</sup>C.-K. Loong, J. W. Richardson, Jr., and M. Ozawa, *J. Catal.* **157**, 636 (1995).
- <sup>3</sup>R. C. Ewing, *Proc. Natl. Acad. Sci. U.S.A.* **96**, 3432 (1999).
- <sup>4</sup>K. Ferguson, *Trans. Am. Nucl. Soc.* **75**, 75 (1996).
- <sup>5</sup>M. A. Subramanian, G. Aravamudan, and G. V. Subba Rao, *Prog. Solid State Chem.* **15**, 55 (1983).
- <sup>6</sup>A. W. Sleight, *Inorg. Chem.* **1968**, 1704; **1969**, 2039.
- <sup>7</sup>F. X. Zhang, J. W. Wang, J. Lian, M. K. Lang, U. Becker, and R. C. Ewing, *Phys. Rev. Lett.* **100**, 045503 (2008).
- <sup>8</sup>R. C. Ewing, W. J. Weber, and J. Lian, *J. Appl. Phys.* **95**, 5949 (2004).
- <sup>9</sup>H. Y. Xiao, F. X. Zhang, F. Gao, M. Lang, R. C. Ewing, and W. J. Weber, *Phys. Chem. Chem. Phys.* **12**, 12472 (2010).
- <sup>10</sup>F. X. Zhang, J. Lian, U. Becker, L. M. Wang, J. Z. Hu, S. Saxena, and R. C. Ewing, *Chem. Phys. Lett.* **441**, 216 (2007).
- <sup>11</sup>F. X. Zhang, J. Lian, U. Becker, R. C. Ewing, J. Z. Hu, and S. K. Saxena, *Phys. Rev. B* **76**, 214104 (2007).
- <sup>12</sup>F. X. Zhang, M. Lang, U. Becker, R. C. Ewing, and J. Lian, *Appl. Phys. Lett.* **92**, 011909 (2008).
- <sup>13</sup>H. Y. Xiao, F. Gao, and W. J. Weber, *Phys. Rev. B* **80**, 212102 (2009).
- <sup>14</sup>N. Garg, K. K. Pandey, C. Murli, K. V. Shanavas, B. P. Mandal, A. K. Tyagi, and S. M. Sharma, *Phys. Rev. B* **77**, 214105 (2008).
- <sup>15</sup>N. R. S. Kumar, N. V. C. Shekar, and P. C. Sahu, *Solid State Commun.* **147**, 357 (2008).
- <sup>16</sup>F. X. Zhang and S. K. Saxena, *Chem. Phys. Lett.* **413**, 248 (2005).
- <sup>17</sup>F. X. Zhang, B. Manoun, S. K. Saxena, and C. S. Zha, *Appl. Phys. Lett.* **86**, 181906 (2005).
- <sup>18</sup>R. S. Kumar, A. L. Cornelius, M. F. Nicol, K. C. Kam, A. K. Cheetam, and J. S. Gardner, *Appl. Phys. Lett.* **88**, 031903 (2006).
- <sup>19</sup>P. R. Scott, A. Midgley, O. Musaev, D. V. S. Muthu, S. Singh, R. Suryanarayanan, A. Revcolevschi, A. K. Sood, and M. B. Kruger, *High Press. Res.* **31**, 219 (2011).
- <sup>20</sup>S. Surble, S. Heathman, P. E. Raison, D. Bouexiere, K. Popa, and R. Caciuffo, *Phys. Chem. Miner.* **37**, 761 (2010).
- <sup>21</sup>Q. Fu, H. Saltsburg, and M. Flytzani-Stephanopoulos, *Science* **301**, 935 (2003).
- <sup>22</sup>G. A. Deluga, J. R. Salge, L. D. Schmidt, and X. E. Verykios, *Science* **301**, 993 (2004).
- <sup>23</sup>J. A. Rodriguez, S. Ma, P. Liu, J. Hrbek, J. Evans, and M. Parez, *Science* **318**, 1757 (2007).
- <sup>24</sup>S. Arai, S. Muto, T. Sasaki, Y. Ukyo, K. Kuroda, and H. Saka, *Electrochem. Solid-State Lett.* **9**, E1 (2006).
- <sup>25</sup>J. B. Thomson, A. R. Armstrong, and P. G. Bruce, *J. Solid State Chem.* **148**, 56 (1999).
- <sup>26</sup>J. B. Thomson, A. R. Armstrong, and P. G. Bruce, *J. Am. Chem. Soc.* **118**, 11129 (1996).
- <sup>27</sup>T. Sasaki, Y. Ukyo, K. Kuroda, S. Arai, S. Muto, and H. Saka, *J. Ceram. Soc. Jpn.* **112**, 440 (2004).
- <sup>28</sup>H. Kishimoto, O. Takahisa, S. Otsuka-Yao-Matsuo, K. Ueda, H. Hosono, and H. Kawazoe, *J. Alloys Compd.* **312**, 94 (2000).
- <sup>29</sup>S. N. Achary, S. K. Sali, N. K. Kulkarni, P. S. R. Krishna, A. B. Shinde, and A. K. Tyagi, *Chem. Mater.* **21**, 5848 (2009).
- <sup>30</sup>T. Baidya, M. S. Hegde, and J. Gopalakrishnan, *J. Phys. Chem. B* **111**, 5149 (2007).
- <sup>31</sup>M. Yashima, S. Sasaki, M. Kakihana, Y. Yamaguchi, H. Arashi, and M. Yoshimura, *Acta Crystallogr., Sect. B: Struct. Sci.* **50**, 663 (1994).
- <sup>32</sup>T. Omata, H. Kishimoto, S. Otsuka-Yao-Matsuo, N. Ohtori, and N. Umesaki, *J. Solid State Chem.* **147**, 573 (1999).
- <sup>33</sup>D. Errandonea and F. J. Manjon, *Prog. Mater. Sci.* **53**, 711 (2008).
- <sup>34</sup>Z. Wang, S. K. Saxena, V. Pischedda, H. P. Liermann, and C. S. Zha, *Phys. Rev. B* **64**, 012102 (2001).

- <sup>35</sup>J. K. Dewhurst and J. E. Lowther, *Phys. Rev. B* **64**, 014104 (2001).
- <sup>36</sup>J. M. Leger, P. E. Tomaszewski, A. Atouf, and A. S. Pereira, *Phys. Rev. B* **47**, 14075 (1993).
- <sup>37</sup>H. Ozturk and M. Durandurdu, *J. Am. Ceram. Soc.* **94**, 932 (2011).
- <sup>38</sup>D. Errandonea, D. Santamaria-Perez, T. Bondarenko, and O. Khyzhun, *Mater. Res. Bull.* **45**, 1732 (2010).
- <sup>39</sup>H. K. Mao, J. Xu, and P. M. Bell, *J. Geophys. Res.* **91**, 4673, doi:10.1029/JB091iB05p04673 (1986).
- <sup>40</sup>S. Klotz, J. C. Chervin, P. Munsch, and G. Le Marchand, *J. Phys. D: Appl. Phys.* **42**, 075413 (2009).
- <sup>41</sup>D. Errandonea, R. S. Kumar, J. Ruiz-Fuertes, A. Segura, and E. Haussühl, *Phys. Rev. B* **83**, 144104 (2011).
- <sup>42</sup>A. Dewaele, F. Datchi, P. Loubeyre, and M. Mezouar, *Phys. Rev. B* **77**, 094106 (2008).
- <sup>43</sup>A. P. Hammersley, S. O. Svensson, M. Hanfland, A. N. Fitch, and D. Häusermann, *High Press. Res.* **14**, 235 (1996).
- <sup>44</sup>W. Kraus and G. Nolze, *J. Appl. Crystallogr.* **29**, 301 (1996).
- <sup>45</sup>J. Rodriguez-Carvajal, "FULLPROF: A program for Rietveld refinement and pattern matching analysis," in *Proceedings of the Satellite Meeting on Powder Diffraction of the XV Congress of the International Union of Crystallography*, Toulouse, France, 16–19 July, 1990, p. 127.
- <sup>46</sup>D. Errandonea, Y. Meng, M. Somayazulu, and D. Häusermann, *Physica B* **355**, 116 (2005).
- <sup>47</sup>F. Birch, *J. Geophys. Res.* **83**, 1257, doi:10.1029/JB083iB03p01257 (1978).
- <sup>48</sup>J. M. Pruneda and E. Artacho, *Phys. Rev. B* **72**, 085107 (2005).
- <sup>49</sup>S. O. -Y.O.-Y. Matsuo, T. Omata, N. Izu, and H. Kishimoto, *J. Solid State Chem.* **138**, 47 (1998).
- <sup>50</sup>G. A. Kourouklis, A. Jayaraman, and G. P. Espinosa, *Phys. Rev. B* **37**, 4250 (1988).
- <sup>51</sup>S. J. Duclos, Y. K. Vohra, A. L. Ruoff, A. Jayaraman, and G. P. Espinosa, *Phys. Rev. B* **38**, 7755 (1988).